Effects of Flow Separation on Shuttle Longitudinal Dynamics and Aeroelastic Stability

J. Peter Reding* and Lars E. Ericsson†
Lockheed Missiles & Space Company, Inc., Sunnyvale, Calif.

The longitudinal dynamic and aeroelastic stability characteristics of various shuttle configurations have been investigated at transonic speeds. Wing flow separation dominates the orbiter dynamic stability in a manner that indicates a potential aeroelastic problem for the first torsional mode of the orbiter wing. Throughout the transonic speed range, flow separations of various types are shown to dominate both dynamic and aeroelastic stability of the launch configuration, causing limit cycle oscillations of certain symmetric elastic modes. The limit cycle oscillations threaten the structural integrity in two ways: 1) by outright overstressing of the structure due to large modal deflection, and 2) by fatigue due to the continued flexing of the structure. Fatigue is a more significant consideration for the reusable (100 flights) shuttle than it has been for previous space boosters, especially in view of the coexisting problem of thermocycling.

Nomenclature

A_F = forebody axial force; coefficient $C_{AF}=A_F/(\rho U^2/2)S$
b = wingspan
c = reference length; mean aerodynamic chord
D = damping derivative of elastic body, Eq. (10)
K = spring constant, Eq. (10)
l = characteristic length for separated flow effect
M = freestream Mach number
m = pitching moment; coefficient $C_m=m/(\rho U^2/2)Sc$
N = normal force, coefficient $C_N=N/(\rho U^2/2)S$
$P(t)$ = buffeting force
q = pitch rate
$q(t)$ = normalized coordinate
S = reference area; wing area
t = time
U = freestream velocity
x = horizontal coordinate (Fig. 5)
z = vertical coordinate (Fig. 5)
α = angle of attack
α_0 = trim angle of attack
$\tilde{\alpha}$ = generalized angle of attack
β = phase lag, Eq. (9)
Δ = increment
ξ = dimensionless horizontal coordinate, $\xi=x/c$
ζ = structural damping, fraction of critical
ζ_a = aerodynamic damping, fraction of critical
θ = pitch perturbation angle (Fig. 5)
λ = wavelength
ρ = freestream density
ϕ = normalized modal deflection (Fig. 12)
ϕ' = normalized modal slope (Fig. 12)
ψ = phase angle, $\psi=\omega t$
$\omega,\bar{\omega}$ = circular frequency, $\bar{\omega}=\omega c/U$

Subscripts

A = strake apex
a = attached flow
D = discontinuity
s = separated flow
T = trailing edge of equivalent delta wing
0 = initial condition

Superscripts

$\bar{(\ )}$ = integrated mean value
i = induced, e.g., $\Delta^i C_N$ = separation-induced normal force

Derivative Symbols

ϕ' = $\partial\phi/\partial x$
$\dot{\alpha}$ = $\partial\alpha/\partial t$; $\ddot{q}=\partial^2 q/\partial t^2$
$C_{m\alpha}$ = $\partial C_m/\partial\alpha$
$C_{mq}+C_{m\dot{\alpha}}$ = $C_{m\dot{\theta}}=\partial C_m/\partial(c\dot{\theta}/U)$
$C_{\bar{m}\dot{\theta}}$, $C_{\bar{m}\theta}$ = integrated mean coefficients for nonlinear characteristics defined in Eqs. (7-9)

Presented as Paper 77-116 at the AIAA 15th Aerospace Sciences Meeting, Los Angeles, Calif., Jan. 24-26, 1977; submitted March 14, 1977; revision received July 15, 1977.

Index categories: Aeroelasticity and Hydroelasticity; Nonsteady Aerodynamics; Jets, Wakes, and Viscid-Inviscid Flow Interactions.

*Research Specialist. Member AIAA.
†Consulting Engineer. Associate Fellow AIAA.

Introduction

THE present analysis is the first step toward the development of an automated computational technique for the prediction of the aeroelastic stability of the Space Shuttle launch vehicle. The quasisteady approach is similar to that used so successfully for the Apollo-Saturn booster.[1-4] The technique was mechanized[5] and used routinely to predict the aerodynamic damping of the low-frequency free-free bending modes of the various operational vehicles[6-10] and was extended further to predict the gust penetration response.[11] The present analysis is aimed specifically at defining the critical, time-lag-sensitive flow phenomena and developing means of predicting their dynamic effects. The approach taken was to first examine the rigid-body dynamic stability data[12-15] for the characteristic signature of a flowfield time lag, i.e., opposite static and dynamic nonlinearities (statically stabilizing but dynamically destabilizing, or vice versa). Next, static force, pressure, and flow visualization data were analyzed to determine the causes of these dynamic anomalies. The phenomena were then modeled using quasisteady techniques to predict the dynamic measurements from static wind-tunnel data. Once a satisfactory match with the rigid-body dynamic data was obtained, the analysis was applied to the elastic vehicle. For each phenomenon, the aerodynamic damping was computed for representative modes where the effect was undamping to give an indication of the seriousness of the various unsteady flow effects. It cannot be known if these are worst-case modes without analyzing all modes. Because of the large number of modes that exist for the shuttle launch configuration, a complete final analysis will

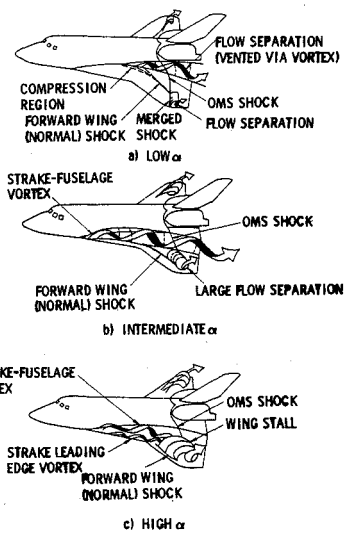

Fig. 1 Sketches of orbiter wing flow for transonic speeds.

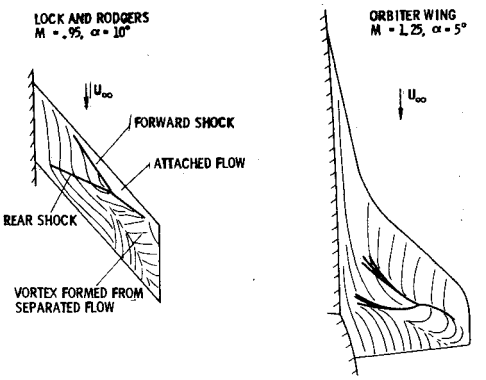

Fig. 2 Comparison of leeside wing flows.

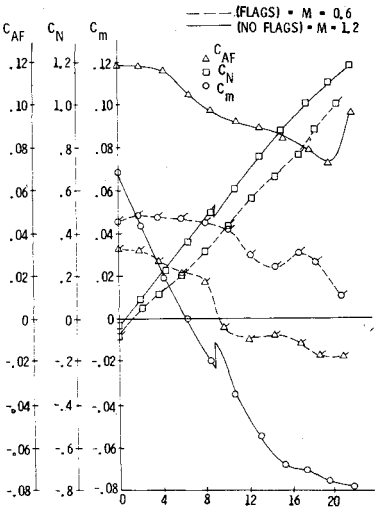

Fig. 3 Typical static data.[23]

have to wait until the procedure is fully computerized. It should be emphasized that in the present context "aeroelastic stability" is used in its dynamic sense and refers to the damping of elastic modes. The forcing function (the fluctuating pressures) is not considered here, as it has been investigated thoroughly by others.[16,17]

The orbiter wing is the major lift-producing element of the launch configuration. Thus, it will dominate the elastic vehicle dynamics. It is natural, therefore, to first consider the unsteady aerodynamics of the orbiter alone without the complication of booster interference. Consequently, the analysis begins with the orbiter-alone vehicle dynamics.

Orbiter Unsteady Aerodynamics

At transonic speeds, the orbiter dynamic stability data[12,13] exhibit the opposition between static and dynamic derivatives which is indicative of a flowfield time lag[1,2,18] (stable $C_{mq}+C_{m\dot{\alpha}}$ excursions correlate with unstable $C_{m\alpha}-\bar{\omega}^2 C_{m\dot{q}}$ excursions, and vice versa). Sharp peaks in the stability derivatives suggest the possibility of highly nonlinear or discontinuous static stability characteristics.[19,20] Oilflow photographs[21] indicate three flow types on the orbiter wing at transonic speeds (Fig. 1). At low angles of attack,‡ the flow is essentially attached with a very small flow separation at the foot of the normal shock on the outboard wing (Fig. 1a). The forward shock appears to emanate from the forward edge of a corner separation at the wing fuselage junction, whereas the OMS pods fix the location of the aft shock (the OMS pods also affect the position of the foward shock via the corner separation, as will be discussed later). At some intermediate angle of attack, the corner separation jumps to the strake apex, and the forward shock also jumps forward quite near the wing leading edge. The wing shock-induced pressure rise couples with the leading-edge suction to produce a large adverse pressure gradient, which causes a large region of flow separation to occur over the outer wing panel (Fig. 1b). Finally, at a high angle of attack, the shock moves all of the way to the leading edge, and the entire outer panel is stalled (Fig. 1c).

It is evident that the flow at the wing-fuselage juncture somehow alters the conventional two-dimensional shock/boundary-layer interaction. Lock and Rogers[22] have described the mechanism whereby conditions at the wing fuselage juncture determine the position of the forward wing shock. The flow component normal to the leading edge is accelerated by expansion over the upper wing surface, and, as a result, the resultant flow is turned toward the fuselage. The flow must eventually be turned parallel to the fuselage. This is accomplished via a compression that coalesces into a single shock—the forward wing shock. The similarity to the orbiter wing flow (although the aft shocks have different origins) is illustrated in Fig. 2. It is the corner separation that furnishes the boundary condition that fixes the forward wing shock on the orbiter. When the separation jumps to the strake apex, the boundary condition for the forward wing shock changes suddenly, causing the shock to jump also.

The corner separation has a duality of character: 1) it acts as the boundary to which the leeside wing flow must adjust itself; and 2) it is vented through a vortex that generates lift over the aft portion of the wing through vortex-induced suction. Thus, it plays a fundamantal role in producing all of the nonlinear stability characteristics illustrated in Fig. 3.[23-25] The discontinuous shock movement caused by the corner separation jump generates the jumps in C_N and C_m at $M=1.2$ (Fig. 3).[23] Although the density of the data points is generally insufficient to define the nonlinearities, the dynamic data[12] are strongly indicative of highly nonlinear or discontinuous static characteristics. The dynamic data were used to define the C_N and C_m jumps shown in Fig. 3 for $M=0.9$ (as will be discussed later). Following the jump, $C_{m\alpha}$ remains stabilizing, and, as the vortex venting the corner separation grows with angle of attack, $C_{m\alpha}$ becomes more stabilizing, whereas $C_{N\alpha}$ increases because of vortex-induced suction over the aft wing.[26,27] Concurrently, C_A plateaus as the vortex suction opposes the usual reduction of C_A with α. Finally, at high α the wing stalls, causing an unstable increment in C_m, a reduction in C_N, and a decrease in C_A. These trends are generally pervasive despite changes in OMS pod configuration.[23-25] At $M=0.6$, the data do not exhibit any discontinuity, since no wing shock occurs at so low a Mach number. However, at $\alpha\approx 8$ deg, an increase in $C_{N\alpha}$ and a

‡The various angle-of-attack regimes (low, intermediate, and high) vary with Mach number, as illustrated in Fig. 4.

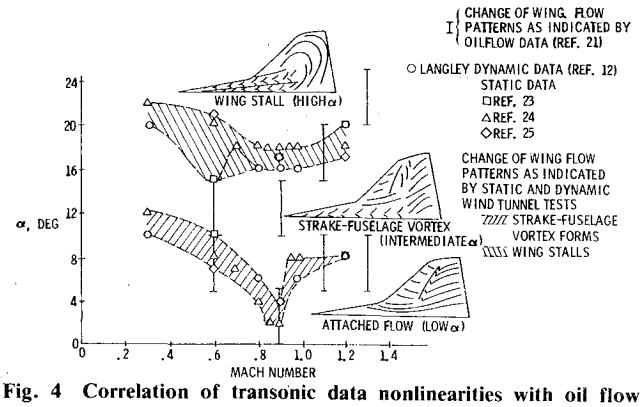

Fig. 4 Correlation of transonic data nonlinearities with oil flow results.

more stable $C_{m\alpha}$ occur due to the effects of the wing-fuselage vortex. At high angles of attack, the stall nonlinearity is also evident. Both static and dynamic stability characteristics exhibit nonlinearities that correlate with the change in flow patterns from oilflow results (Fig. 4), further verifying that the wing flow is responsible for both static and dynamic nonlinearities. (The oilflow photographs were taken at $\Delta\alpha = 5$ deg increments; thus we have the 5-deg data bars in Fig. 4.)

The variation in the flow boundaries in Fig. 4 are largely the result of variations in OMS pod configuration, since the wing flow pattern is sensitive to the OMS pod configuration.[21,28] The OMS pods directly affect the position of the aft wing shock, and indirectly they also affect the position of the forward shock. The OMS pods create an adverse pressure gradient at the wing-fuselage juncture, due to their bow shocks at high transonic speeds and because of stagnation of the pod-induced downwash at lower speeds. The associated pressure rise feeds upstream through the thick viscous layer at the wing-fuselage juncture, affecting the location of the corner separation and thus the forward wing shock. Unfortunately, the OMS pod configuration is the most changed configuration feature of the orbiter. It seems to be different for nearly every wind-tunnel test. Of the static tests, the OMS pod configuration in Ref. 23 is the one most like the pods of the dynamic model.[12,13]

Orbiter Rigid-Body Dynamics

All evidence indicates that the strake-fuselage vortex dominates the orbiter wing loads at transonic speeds for a large-angle-of-attack range. Regardless of whether it is the discontinuous shock jump or the suction effect of the vortex, the nonlinear wing load is a function of the corner separation. For a first approximation, it was assumed that the crossflow at the strake apex determines the boundary-layer condition at the wing-fuselage juncture and thus the corner separation extent. When the separation occurs at the strake apex. the situation is similar to that for free-body vortices on slender bodies of revolution.[29] For the shuttle, this means that the crossflow at the strake apex determines the position of the corner vortex relative to the aft wing, thus determining the aft wing lift. At high angles of attack, the strake and main wing vortices combine into one vortex (Fig. 1c). This rolled-up vortex is swept to the outboard wing panel, where it bursts at stall. Thus, all of the nonlinearities in the stability derivatives are determined by crossflow at the strake apex. In the dynamic case the induced load, the nonlinear increment, will lag the vehicle attitude due to the finite convection speed of the vortices.[30] That is, the induced pitching moment is a function of the angle of attack at the strake apex at an earlier time.[26,27]

$$\Delta^i C_m = \Delta^i C_{m\alpha}\alpha_A(t-\Delta t) \tag{1a}$$

$$\Delta t = \frac{x_A - x_s}{\bar{U}} = c\frac{(\xi_A - \xi_s)}{\bar{U}} \tag{1b}$$

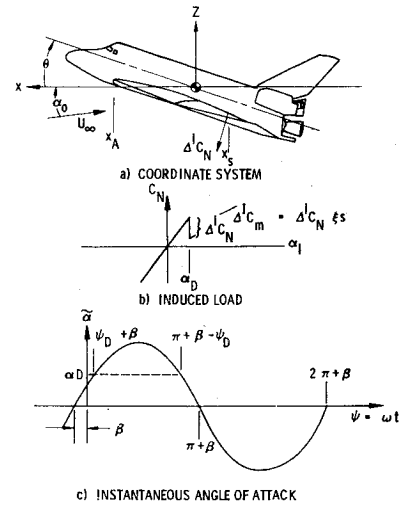

Fig. 5 Rigid-body definitions.

where x_A is the apex station, x_s is the induced load station, and $\bar{U} = U$ is the convection speed of the vortex.[26,27] With the definitions in Fig. 5,

$$\tilde{\alpha} = \alpha_0 + \theta - (\dot{z}/U) \tag{2}$$

$$\tilde{\alpha}_A(t-\Delta t) = \alpha_0 + \theta(t-\Delta t) - c\xi_A\dot{\theta}(t-\Delta t)/\bar{U} \tag{3}$$

For harmonic oscillations, $\theta(t) = \Delta\theta e^{i\omega t}$. Thus,

$$\theta(t-\Delta t) = \theta(t)\cos(\omega\Delta t) - [\dot{\theta}(t)/\omega]\sin(\omega\Delta t) \tag{4a}$$

$$\dot{\theta}(t-\Delta t) = \theta(t)\cos(\omega\Delta t) - [\ddot{\theta}(t)/\omega]\sin(\omega\Delta t) \tag{4b}$$

where the $\ddot{\theta}$ term can be neglected for low reduced frequencies, $\bar{\omega}^2 \ll 1$. Combining Eqs. (1-4) and taking the derivative gives

$$\Delta^i C_{m\dot{\theta}} = \frac{\partial \Delta^i C_m}{\partial(\dot{\theta}c/U)} = -\Delta^i C_{m\alpha}\left[\frac{\sin(\omega\Delta t)}{\omega} + \xi_A\cos(\omega\Delta t)\right] \tag{5a}$$

$$\bar{\omega} = \omega c/U \quad \Delta^i C_{m\alpha} = C_{m\alpha} - C_{m\alpha a} \tag{5b}$$

The induced damping derivative is added to the attached flow damping derivative for angles of attack where the strake-fuselage vortex occurs:

$$(\alpha < \alpha_v) \quad \frac{\partial C_m}{\partial(\dot{\theta}c/U)} = \frac{C_{m\dot{\theta}a}}{2(\dot{\theta}c/U)} = -C_{N\alpha a}\xi_T^2 \tag{6a}$$

$$(\alpha \geq \alpha_v) \quad \frac{\partial C_m}{\partial(\dot{\theta}c/U)} = \frac{\Delta^i C_{m\dot{\theta}}}{\partial(\dot{\theta}c/U)} + \frac{C_{m\dot{\theta}a}}{\partial(\dot{\theta}c/U)} \tag{6b}$$

ξ_T is the trailing-edge location of the equivalent slender delta wing.[26,27] Equations (5) and (6) can be used to estimate the orbiter damping as long as the induced pitching moment derivative is finite and constant; however, when the corner seperation jumps, $\Delta^i C_{m\alpha} = \infty$. An equivalent static moment derivative can be defined by integrating the discontinuous moment curve over the oscillation amplitude[31]:

$$C_{\bar{m}\theta} = \frac{1}{\Delta\theta^2}\int_{-\Delta\theta}^{\Delta\theta} C_m\,d\theta = C_{m\alpha a} + \frac{\Delta C_m}{\Delta\theta}\left[1 - \frac{\alpha_D - \alpha_0}{\Delta\theta}\right] \tag{7}$$

provided that $\alpha_0 \leq \alpha_D \leq \alpha_0 + \Delta\theta$. ΔC_m is the moment discontinuity and $\Delta\theta$ the oscillation amplitude; likewise, the equivalent damping derivative is defined by integrating over the oscillation cycle[31]:

$$C_{\bar{m}\dot{\theta}} = \frac{1}{\pi\Delta\theta\bar{\omega}}\int_{\psi_0}^{\psi_0+2\pi} C_m(\psi)\cos\psi\,d\psi \tag{8}$$

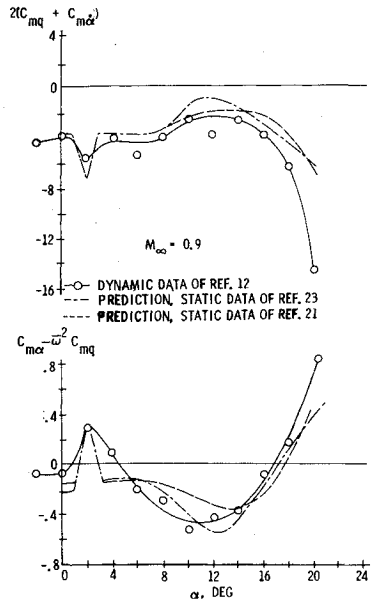

Fig. 6 Comparison of quasisteady predictions with orbiter dynamic stability data at $M = 0.9$.

where $\psi = \omega t$ and $2\pi = \omega T$; T is the period of oscillation (Fig. 5c). This gives[31]

$$C_{m\dot{\theta}} = C_{m\dot{\theta}a} - (2\Delta C_m / \pi\bar{\omega}\Delta\theta)\,[\sin\beta\cos\psi_D] \qquad (9)$$

where

$$\psi_D = \sin^{-1}\left[\frac{\alpha_D - \alpha_0}{\Delta\theta}\cos\beta\right] \qquad \tan\beta = \left[\frac{\sin\omega\Delta t}{\bar{\omega}} + \xi_A\cos\omega\Delta t\right]\bar{\omega}$$

The magnitude of the moment discontinuity (ΔC_m) was estimated from the spikes in $C_{m\alpha} - \bar{\omega}^2 C_{mq}$ from the dynamic test data (e.g., at $\alpha = 2$ and 8 deg at $M = 0.9$, Fig. 6) using Eq. (9) (where $\Delta\theta = 1$ deg).§ These values were then substituted in Eq. (9) to obtain the damping spikes. The rest of the damping curve was computed using the static data of Ref. 23, since that OMS configuration best approximates the OMS configuration of the dynamic model. In Fig. 6, the results of these estimates are compared with the Langley damping measurements.[12] The agreement is gratifying, since it verifies the flow model, showing that the quasisteady analyses technique can provide the analytic tool for predicting the full-scale dynamic effects of separated flow from static data. This is particularly important, since the separated flow phenomena that dominate the orbiter wing flow are extremely Reynolds number sensitive, and the dynamic wind-tunnel data are for Reynolds numbers two to three orders of magnitude below flight. It is not possible to simulate full-scale Reynolds number effects in dynamic wind-tunnel tests using boundary-layer trips when separated flow is involved. Trips tend to alter the all-important time-lag effects and even the dynamic separation pattern.[32] Once the full-scale static aerodynamic characteristics are obtained from tests performed at various Reynolds numbers and with boundary-layer trips, the dynamic characteristics can be predicted using quasisteady techniques. This analytic extrapolation technique is similar to the approach used so successfully on the first manned space vehicles[1-10] and should be useful for both the orbiter dynamic stability and the aeroelastic stability (as will be discussed in the following sections).

Launch Configuration Dynamics

Rigid-body pitch damping data for the launch configuration[14] also exhibit the characteristic signature of a flowfield time lag. At $M = 1.2$, a large undamping peak at

§This is how the discontinuities in Fig. 3 were obtained.

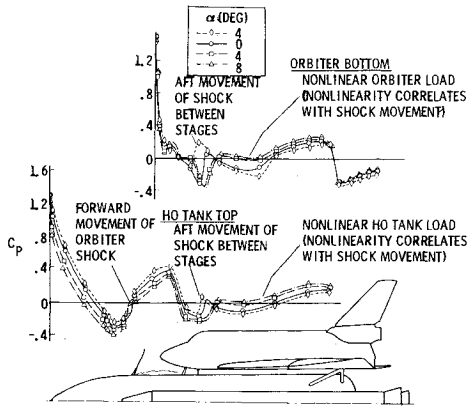

Fig. 7 Pressure distributions between stages of launch configuration at $M = 1.2$.

$\alpha = 2.2$ deg suggests a pitching moment discontinuity. Pressure distribution data[33] and shadowgraph photographs[27] indicate that the probable cause is a region of flow separation on the HO tank due to the detached orbiter bow shock. Pressure distribution data[33] illustrate how this separation responds to angle of attack (Fig. 7). Crossflow over the HO tank nose forward of separation results in a thickening of the leeside boundary layer which, in turn, causes a forward movement of the separation point. The terminal normal shock standing between the orbiter and HO tank exhibits an aft movement that correlates with the forward movement of the orbiter bow shock (Fig. 7). Likewise, the static pressures aft of the shock on both the HO tank top and the orbiter bottom exhibit a nonlinearity that correlates with the shock movement. Thus, the entire flowfield is coupled. This is the first indication that the flow between the stages is somewhat analogous to inlet flow.[34]

The position of the normal shock between the stages is determined by the mass flow that can be accommodated by the more or less two-dimensional channel between the stages from the strake apex aft to the HO tank base. Any excess mass flow must be spilled laterally upstream of the strake. The flow upstream of the orbiter bow shock is aligned axially, and spilling begins aft of the shock. The spilling is a function of the pressure distribution over the top of the HO tank. When the pressures are high, a relatively large amount of mass flow is forced out laterally. However, when the pressure drops, as it does under the orbiter nose, the outflow decreases. When the orbiter bow shock is in its aft position, the area of high pressure is reduced, and less mass flow is spilled. In order to get rid of the excess mass flow, the normal shock between stages moves forward, giving an additional high-pressure region forward of the strakes, which spills the excess mass flow. Of course this does not happen instantaneously; a considerable time lag is involved. The effect of an angle-of-attack change first must be convected downstream to the orbiter bow shock before the separation point can move. The excess mass flow then must be convected into the "inlet," and the "inlet" must fill before the normal shock is forced forward to the new equilibrium position. This filling time can be quite long, especially when one considers the considerable area for venting between the stages.

It should be noted that removing the solid rocket motors (SRM's) eliminates the nonlinearity in the damping derivative for the launch configuration. The SRM's restrict the spilling of flow around the HO tank which is essential for establishment of the "inlet" flow. In addition, the SRM bow shocks merge with the displaced orbiter bow shock, promoting flow separation.[28]

Launch Configuration Rigid-Body Dynamics

It is impossible to estimate the time lag theoretically. However, the combination of static pressure data, dynamic

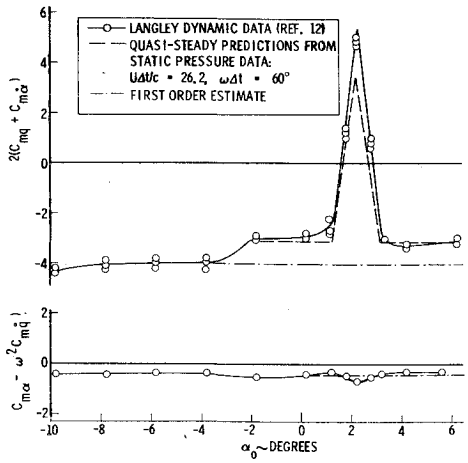

Fig. 8 Comparison of quasisteady predictions with launch configuration dynamic moment derivative measurements at $M=1.2$

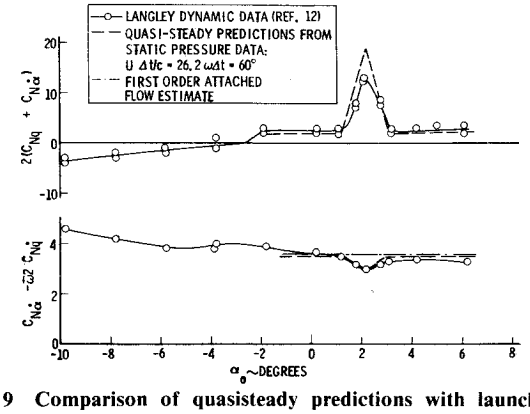

Fig. 9 Comparison of quasisteady predictions with launch configuration dynamic normal force derivative measurements at $M=1.2$.

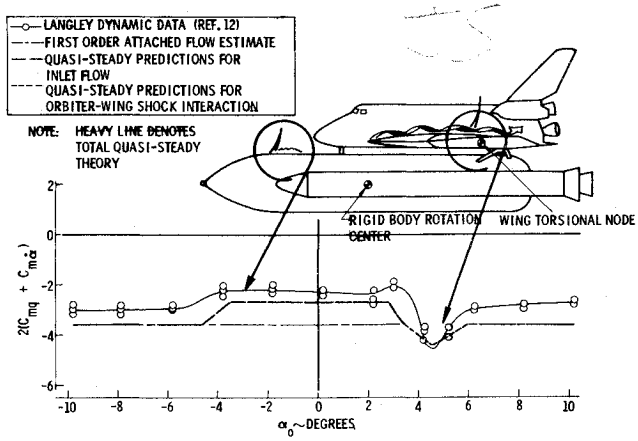

Fig. 10 Effect of HO tank separation and wing shock interaction on launch configuration rigid-body damping ($M=0.9$).

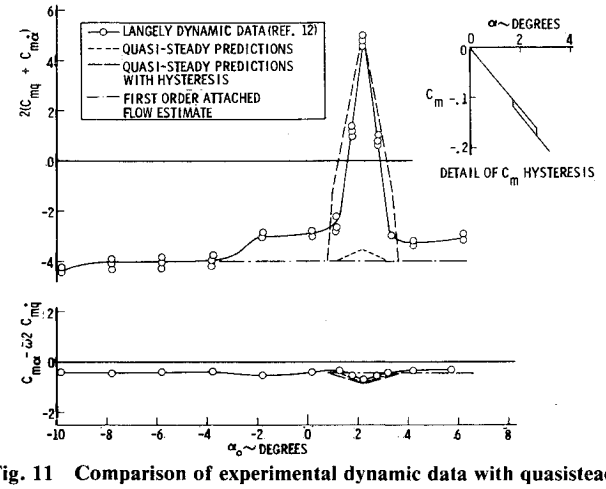

Fig. 11 Comparison of experimental dynamic data with quasisteady predictions assuming only sudden separation effects ($M=1.2$).

stability data, and quasisteady theory supplies the tools necessary for estimating the time lag. If both the static and dynamic effects of the discontinuity are known, Eq. (9) can be used to estimate the time lag Δt. This has been done for $M=1.2$ using an iterative procedure. The jump increment was first taken in reference to the attached flow level to obtain a first estimate of the time lag. Then the plateau level for $\alpha \geq -2$ deg, on both sides of the undamping peak (Fig. 8), was computed. The jump was then incremented from the plateau and a second time lag determined. After just two iterations, the results shown in Figs. 8 and 9 were obtained. The load jumps and the effect of the continuous shock movement were estimated by integrating the pressure data of Ref. 33. The very long time lag (the vehicle travels 26.2 chord lengths during Δt) is not unreasonable for inlet flows.[34] The good agreement with the Langley results is strong evidence that the flow model is valid.

Actually, the time lag will be different for the various load components. However, for the rigid body, much of the loading between the orbiter and the booster has zero net effect dynamically as the various positive and negative loads cancel each other. As a result, the load induced by the orbiter bow shock dominates, and the single lumped time-lag approach successfully predicts the rigid-body dynamics. In contrast, the single lumped time-lag approach will not be sufficient for the computation of the aeroelastic stability. The effects of the various loads between the stages will not necessarily cancel each other; rather, they are likely to be additive and thus dominate the vehicle dynamics.

The inlet flow effect is not restricted to $M=1.2$ but occurs over the Mach number range $0.9 \leq M \leq 1.4$.[27,33] However, at $M=0.9$ the discontinuity in the shock position is not present, since the shock stands so close to the shoulder. This explains why no undamping peak appears in the $M=0.9$ dynamic data (Fig. 10), although the plateau is present. The plateau is well predicted from the static induced derivatives (from the integrated pressure data) with $\omega\Delta t=60$ deg. Evidence of the strake-fuselage vortex effect is also present in the $M=0.9$ data. The damping spike is well predicted if one assumes that the wing shock jumps at $\alpha=4.5$ deg rather than at $\alpha=2.2$ deg, as it did for the orbiter alone. Evidently, flow-straightening effects of the HO tank and SRM's reduce the crossflow at the strake apex so that the corner separation jump does not occur until $\alpha=4.5$ deg.

Another, simpler flow model was postulated earlier in the study. It was assumed that the induced loads did not involve an inletlike flow. Rather, the orbiter bow shock was treated as a simple terminal normal shock with only boundary-layer convection and accelerated-flow time lag.[19,20] If a large (0.7 deg) amplitude hysteresis loop was assumed, the undamping peak at $M=1.2$ could be predicted (Fig. 11). However, the plateau level could not be predicted using the continuous separation movement, because the time lag was too small. Although the results are not conclusive, the evidence so far supports the inlet flow model.

Aeroelastic Stability

The equation of motion of the elastic vehicle describing single-degree-of-freedom bending oscillations can be written[2] as

$$\bar{m}\{\ddot{q}(t)+2\omega[\zeta-(B/2\omega U)(D_s+D_a)]\dot{q}(t)+\omega^2[1-(B/\omega^2)(K_s+K_a)]q(t)\}=P(t) \qquad (10)$$

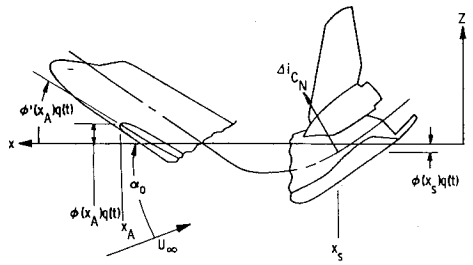

Fig. 12 Coordinate system for elastic orbiter.

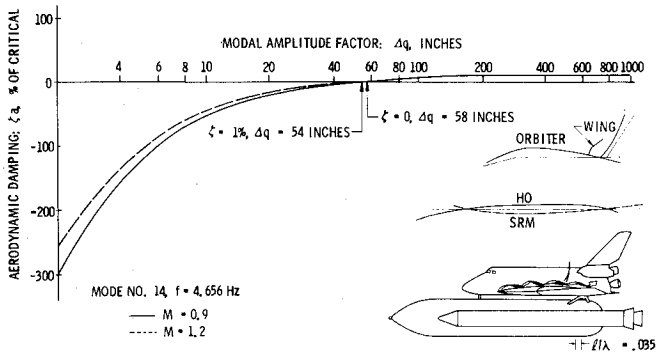

Fig. 13 Effect of orbiter wing shock jump on the aerodynamic damping of the launch configuration mode 14.

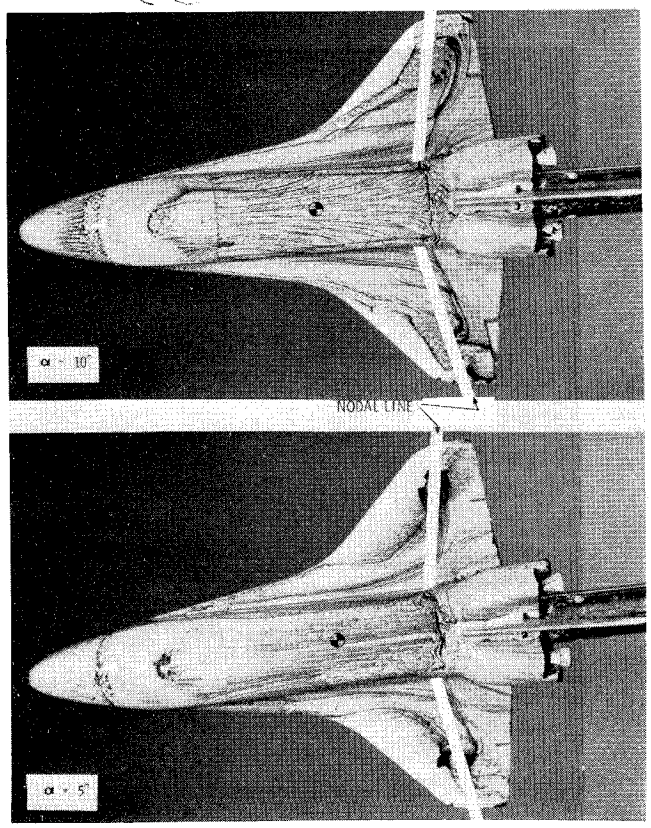

Fig. 14 Correlation of wing torsional mode node line with orbiter wing flow patterns ($M=1.2$).

where $P(t)$ is the buffeting force input.

One requirement for stability is that the coefficient $\dot{q}(t)$ cannot be negative, i.e.,

$$\zeta-(B/2\omega U)(D_s+D_a)\geq 0 \tag{11}$$

where D_s and D_a are the aerodynamic damping derivatives in separated and attached flow, respectively (a negative coefficient is damping). ζ is the structural damping as a fraction of critical, and $-B/2\omega U=-\rho US/4\omega\tilde{m}$ puts the aerodynamic damping into the same form as the structural damping. For a discontinuous aerodynamic load, the damping is obtained by integrating over one cycle similar to what was done for the rigid-body damping[19,20]:

$$D_s=\frac{\phi(\xi_s)c}{\pi\Delta q\tilde{\omega}}\int_{\beta}^{2\pi+\beta}C_N(\psi)\cos\psi d\psi \tag{12}$$

For the discontinuous wing load illustrated in Fig. 5, the generalized angle of attack is still

$$\tilde{\alpha}=\alpha_0+\theta-(\dot{z}/U) \tag{13}$$

The jump effect is the result of conditions at the strake apex at the time $(t-\Delta t)$. Therefore,

$$\tilde{\alpha}(t-\Delta t)=\alpha_0+\theta_A(t-\Delta t)-\dot{z}_A(t-\Delta t)/U \tag{14}$$

With the elastic body coordinate system (Fig. 12),

$$\theta_A(t-\Delta t)=\phi'(\xi_A)q(t-\Delta t) \tag{15a}$$

$$\dot{z}_A(t-\Delta t)=\phi(\xi_A)\dot{q}(t-\Delta t) \tag{15b}$$

From Ref. 27, the induced aerodynamic damping derivative is

$$\bar{D}_s=-\frac{2\phi(\xi_s)c}{\pi\Delta q\tilde{\omega}}\Delta C_N\sin\beta\cos\psi_D \tag{16a}$$

$$\beta=\tan^{-1}\left\{\frac{\phi'(\xi_A)\sin\omega\Delta t+\phi(\xi_A)(\omega/U)\cos\omega\Delta t}{\phi'(\xi_A)\cos\omega\Delta t-\phi(\xi_A)(\omega/U)\sin\omega\Delta t}\right\} \tag{16b}$$

$$\psi_D=\sin^{-1}\left\{\frac{(\alpha_D-\alpha_0)\cos\beta}{\Delta q[\phi'(\xi_A)\cos\omega\Delta t-\phi(\xi_A)(\omega/U)\sin\omega\Delta t}\right\} \tag{16c}$$

The aerodynamic damping is

$$\zeta_a=(\rho US/4\omega\tilde{m})[\bar{D}_s+D_a] \tag{17}$$

where $D_a=-C_{N\alpha}[\phi(\xi_T)]^2$. $C_{N\alpha}$ is the attached flow normal derivative of the boost configuration.[35]

Some discussion of the limits of applicability of the quasisteady theory is appropriate before presenting results of the analysis. A simple description of the limits of the technique is given in Ref. 36. It shows clearly that, as long as the wavelength λ of the interference effect is large relative to the characteristic dimension l of the effected body element, the quasisteady technique is valid, i.e., when $l/\lambda\leq 0.25$, which is the case for the present analysis (as indicated in the relevant mode shape sketches).

From Eq. (16), one can see that, when the vehicle is describing infinitesimal amplitude oscillations (Δq) at $\alpha_0=\alpha_D$ with $\psi_D=0$, the induced damping $\bar{D}_s\to\infty$. As the oscillation amplitude increases, $\bar{D}_s$ becomes finite. Limit cycle oscillations will occur for modes such as the one shown in Fig. 13 when the coefficient of $\dot{q}(t)$ in Eq. (10) is zero. If the structural damping is zero, $\zeta=0$ in Eqs. (11) and (17), limit cycle oscillations occur at $\bar{D}_s+D_a=0$ (Fig. 13). A more realistic value of the structural damping is $\zeta=0.01$; therefore, a limit cycle oscillation occurs where $\zeta_a=-0.01$.

Limit cycle oscillations occur for the fourteenth mode of the shuttle liftoff configuration at $M=0.9$ and 1.2 (Fig. 13). This limit cycle value is conservative in the sense that it may not have time to develop due to the continually changing flow conditions throughout ascent. However, it is unconservative in the sense that no coupling with other modes has been included. To determine exactly how large the maximum amplitude will be requires a more complete modal analysis.

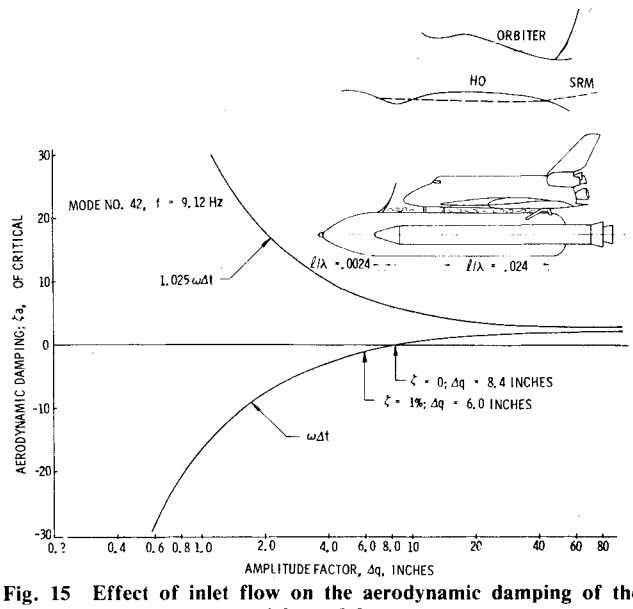

Fig. 15 Effect of inlet flow on the aerodynamic damping of the launch configuration at $M = 1.2$, $\alpha = 2.2$ deg.

Rather late in the study, the work of Chipman and Rauch[37] became available to the authors. Although their analysis revealed no aeroelastic instabilities at $\alpha = 0$, the location of the node line of the first torsional mode gives reason for concern in regard to the wing shock jump at $\alpha > 0$. Figure 14 shows the nodal line superimposed on $M = 1.2$ oil flow photographs. The shock moves forward of the node line with increasing angle of attack. The negative shock-induced load will be aerodynamically undamping when it is forward of the node. The statically destabilizing jump load was damping for rigid-body oscillations (Fig. 10). However, the sign of the jump moment about the wing torsion node is reversed, and it will therefore cause undamping. Time did not permit an analysis of the torsional mode; however, it appears that at the very least limit cycle oscillations are possible in the range $0.9 \leq M \leq 1.2$, when the wing shock jump occurs. How critical these limit cycle oscillations will be for the wing structural integrity can only be determined through further analysis.

The inlet flow between orbiter and booster involves massive discontinuous loads, which could certainly result in limit cycle oscillations for critical modes. The use of one single integrated mean time lag is likely to introduce large errors in the aeroelastic analysis because of the possible dominance of the interstage loads. The situation is aggravated further by the fact that the elastic-body frequencies are much higher than the rigid-body frequency. This is illustrated in Fig. 15. It takes a change of only 2.5% in the mean time lag $\bar{\Delta}t$ to change the results from undamping with limit cycle oscillations to damping for all amplitudes. The "inlet walls" make 20 pulsations during the time lag $\bar{\Delta}t$. As the threat to the structural integrity of the launch configuration posed by the inletlike flow and the associated discontinuous flow change is fairly obvious, the results in Fig. 15 serve not as much to demonstrate the possibility of limit cycle oscillations as to illuminate the need for a more sophisticated analysis. With more accurate information about the time lag for the various interstage loads, obtained experimentally, the present quasisteady analysis technique should be able to predict more realistic aeroelastic characteristics. Note that, although the large time lag causes a 20-cycle phase lag, the quasisteady technique is still valid, i.e., $\ell/\lambda < 0.25$ (see Fig. 15). However, the long time lag may make it necessary to consider the environmental, trajectory-dependent transients.

Conclusions

An exploratory analysis of the effects of flow separation on the dynamic and aeroelastic stability of various shuttle configurations has shown the quasisteady technique to be a valuable tool for predicting full-scale vehicle dynamics. The analysis has identified two unsteady transonic flow phenomena that could cause undamping of certain critical free-free bending modes: 1) wing shock jump, and 2) inletlike flow between stages.

Both effects involve discontinuous aerodynamics that result in limit cycle oscillations of certain critical free-free bending modes. The wing shock jump affects both booster bending modes and orbiter wing torsional modes. It clearly poses a real threat to the structural integrity of the space shuttle. Much less obvious is the mechanism through which the interstage inletlike flow may endanger the structural integrity of the boost configuration. The potential threat can only be determined through further, more detailed analysis. Perhaps the most useful experimental information could be obtained from a fluctuating pressure test of the flow between the stages. Coherence results could show conclusively the coupling of the inlet flow and would furnish accurate convection speed measurements that could be applied to the computation of the modal damping of the flight vehicle via quasisteady techniques.

The separation-induced limit cycle oscillations threaten the structural integrity in two ways: either by outright overstressing the structure due to large modal deflections or via fatigue. Fatigue is a much more serious problem for the reusable shuttle orbiter than it was for the single-flight Apollo-Saturn vehicles. Since limit cycle oscillations will affect fatigue life, a complete modal analysis is recommended to define the limit cycles for all critical modes.

All of the unsteady separated flow phenomena will be sensitive to Reynolds number. The quasisteady theory relies on static wind-tunnel data, which usually are obtained for Reynolds numbers two or three orders of magnitude below the flight value. Thus, the effect of Reynolds number on the induced loads must be understood to allow extrapolations to full scale. It is recommended that the effects of Reynolds number on these critical unsteady flow mechanisms be investigated, since simulation of full-scale Reynolds number rarely is possible. Systematic tests performed at various Reynolds numbers with boundary-layer tripping devices of various designs (location, etc.) could provide the information needed for prediction of full-scale unsteady flow from subscale model data.

Acknowledgment

The results presented herein were obtained in a study for NASA, Contract NAS 8-30652, under the direction of W.W. Clever, NASA Marshall Space Flight Center, J.C. Young, NASA Johnson Space Center.

References

[1]Ericsson, L.E. and Reding, J.P., "Report on Saturn I—Apollo Unsteady Aerodynamics," LMSC/A650215, Feb. 1964.

[2]Ericsson, L.E. and Reding, J.P., "Analysis of Flow Separation Effects on the Dynamics of a Large Space Booster," *Journal of Spacecraft and Rockets*, Vol. 2, July-Aug. 1965, pp. 481-490.

[3]Rainey, A.G., "Progress on Launch Vehicle Buffeting Problem," *Journal of Spacecraft and Rockets*, Vol. 2, May-June 1965, pp. 289-299.

[4]Hanson, P.W. and Dogget, R.V. Jr., "Wind Tunnel Measurements of Aerodynamic Damping Derivatives of a Launch Vehicle Vibrating in Free-Free Bending Modes at Mach Numbers from 0.7 to 2.87 and Comparison with Theory," NASA TN D-1391, 1962.

[5]Davis, N.L., "Computer Program for Quasi-Steady Aeroelastic Analysis," Lockheed Missiles & Space Co., LMSC M-3767-3, Dec. 1967.

[6]Ericsson, L.E. and Reding, J.P., "Technical Summary Report, Aeroelastic Characteristics of Saturn IB and Saturn V Launch Vehicles," Lockheed Missiles & Space Co., LMSC M-37-67-5, Dec. 1967.

[7]Davis, N.L., "The Aeroelastic Characteristics of the Saturn V Launch Vehicle SA-505," LMSC M-30-69-2A, April 1969.

[8]Davis, N.L., "The Aeroelastic Characteristics of the Saturn V Launch Vehicles, SA-506 and an Updated SA-505," Lockheed Missiles & Sace Co., LMSC N-3C-69-2B, June 1969.

[9]Davis, N.L., "The Aeroelastic Characteristics of the Saturn V Launch Vehicle SA-507 for Launch Dates of 14 November and 16 November, 1969," Lockheed Missiles & Space Co., LMSC N-36-69-2C (2nd Addendum to LMSC N-3C-69-2A), Oct. 1969.

[10]Davis, N.L., "The Aeroelastic Characteristics of the Saturn V Launch Vehicle SA-508 for April 1970 Launch Date," Lockheed Missiles & Space Co., LMSC M-3C-69-2D (3rd Addendum to LMSC Report N-36-29-2A), Oct. 1969.

[11]Ericsson, L.E., Reding, J.P., and Guenther, R.A., "Elastic Launch Vehicle Response to Sinusoidal Gusts," *Journal of Spacecraft and Rockets,* Vol. 10, April 1973, pp. 244-252.

[12]Boyden, R.P. and Freeman, D.C., "Subsonic and Transonic Dynamic Stability Derivatives of a Modified 089B Shuttle Orbiter," NASA TMX 72631, Dec. 1974.

[13]Freeman, D.C. Jr., Boyden, R.D., and Davenport, E.E., "Supersonic Dynamic Stability Derivatives of a Modified 089B Shuttle Orbiter," NASA TMX 72631, Dec. 1974.

[14]Freeman, D.C. Jr., and Boyden, R.P., and Davenport, E.E., "Subsonic and Transonic Dynamic-Stability Characteristics of the Space Shuttle Launch Vehicle," NASA TMX-336, March 1976.

[15]Boyden, R.P., Freeman, D.C. Jr., and Davenport, E.E., "Supersonic Dynamic-Stability Derivatives of the Space Shuttle Launch Vehicle," NASA TMX-3315, Feb. 1976.

[16]Dods, J.B. Jr and Hanley, R.D., "Inflight Aeroacoustic Environments of Prospective Space Shuttle Vehicles," NASA TMX-2570, July 1972.

[17]Hanly, R.D., "Surface-Pressure Fluctuations Associated with Aerodynamic Noise on the Space Shuttle Launch Configuration at Transonic and Supersonic Speeds," *Proceedings of the AIAA/ASME/SAE 17th Structures, Structural Dynamics, and Materials Conference,* King of Prussia, Pa., May 5-7, 1976, pp. 241-247.

[18]Ericsson, L.E. and Reding, J.P., "Dynamics of Separated Flow over Blunt Bodies," NASA CR-76912, Tech. Summary Rept., Dec. 1965.

[19]Ericsson, L.E., "Aeroelastic Instability Caused by Slender Payloads," *Journal of Spacecraft and Rockets,* Vol. 6, Dec. 1969, pp. 1404-1409.

[20]Ericsson, L.E., French, N.J., and Guenther, R.A., "The Aeroelastic Characteristics of the Saturn 1B Launch Vehicle with Biconic Payload Shroud," Lockheed Missiles & Space Co., LMSC M-37-67-1, July 1967.

[21]Nichols, M.E., "Results of Investigation on the 0.004-scale model 74-0 of the Configuration 4 (Modified) Space Shuttle Orbiter in the NASA/MSFC 14 by 14 inch, Trisonic Wind Tunnel (0A131)," NASA CR 141, 521, March 1975.

[22]Lock, R.C. and Rogers, E.W.E., "Aerodynamic Design of Swept Wings and Bodies for Transonic Speeds," *Proceedings of 2nd International Congress of Aeronautical Sciences,* 1960.

[23]Allen, E.C. and Lindhall, R.H., "Investigation in the MSFC TWT to verify the Static Stability and Control Effectiveness of the 0.004-Scale Model (74-0) of the Shuttle 5 Orbiter (0A-108)," NASA CR 141,537, June 1975.

[24]Sparks, V.H. and Moser, M.M. Jr., "Wind Tunnel Tests on an 0.015-Scale Configuration 140 A1B Space Shuttle Orbiter Model (67-0) in the NASA LRC 8-foot TPT to Obtain Transonic Aerodynamic Force Data (0A-106)," NASA CR 134,426, June 1975.

[25]Hardin, R.B. and Burrows, R.R., "Wind Tunnel Tests of an 0.019-Scale Space Shuttle Integrated Vehicle in the NASA Ames 8×7-foot Unitary Wind Tunnel (1A-120)," NASA CR 141,518, April 1975.

[26]Ericsson, L.E. and Reding, J.P., "Unsteady Aerodynamic Flow Field Analysis of the Space Shuttle Configuration, Part I: Orbiter Aerodynamics," NASA CR-144332, April 1976.

[27]Reding, J.P. and Ericsson, L.E., "Unsteady Aerodynamic Flow Field Analysis of the Space Shuttle Configuration, Part II: Launch Vehicle Aeroelastic Stability," NASA CR-144333, April 1976.

[28]Reding, J.P. and Ericsson, L.E., "Unsteady Aerodynamic Analysis of Space Shuttle Vehicles, Part III: Booster interference Effects," NASA CR-120124, Aug. 1973.

[29]Schiff, L.B. and Tobak, M., "Results from a New Wind-Tunnel Apparatus for Studying Coning and Spinning Motions on Bodies of Revolution," *AIAA Journal,* Vol. 8, Nov. 1970, pp. 1953-1957.

[30]Lamborne, N.C., Bryer, D.W., and Maybery, J.F.M., "A Preliminary Note on the Behvaior of the Leading-Edge Vortices of a Delta Wing Following a Sudden Change in Incidence," National Physical Lab., NPL Aero. Note 1006, March 13, 1962.

[31]Ericsson, L.E., "Separated Flow Effects on the Static and Dynamic Stability of Blunt Nosed Cylinder Flare Bodies," NASA CR-76919, Dec. 1965.

[32]Ericsson, L.E. and Reding, J.P., "Scaling Problems in Dynamic Tests of Aircraft-Like Configurations," *AGARD Symposium on Unsteady Aerodynamics,* Ottawa, Canada, Sept. 26-28, 1977; paper 24 in AGARD CP-227.

[33]Gillins, R.L., "Airloads Investigation of a 0.030-Scale Model of the Space Shuttle Launch Vehicle 140A1B Launch Configuration (Model 47-OTS) in the ARC 11-foot Unitary Plan Wind Tunnel for Mach Range 0.6 to 1.4 (1A14A)," NASA CR 134-445, March 1975.

[34]Dailey, C.E., "Supersonic Diffuser Stability," *Journal of the Aeronautical Sciences,* Vol. 22, Nov. 1955, pp. 733-749.

[35]Bisplinghoff, R.L., Ashley, H., and Halfman, R.L., *Aeroelasticity,* Addison-Wesley, Cambridge, Mass., 1955, pp. 418-419.

[36]Reding, J.P. and Ericsson, L.E., "Aeroelastic Stability of the 747/Orbiter", *Journal of Aircraft,* Vol. 14, Oct. 1977, pp.988-993.

[37]Chipman, R.R. and Rauch, F.J., "Analytical and Experimental Study of the Effects of Wing-Body Aerodynamic Interference on Space Shuttle Subsonic Flutter," NASA CR-2488, Jan. 1975.

Announcement: 1977 Author and Subject Index

The indexes of the five AIAA archive journals (*AIAA Journal, Journal of Aircraft, Journal of Energy, Journal of Hydronautics, Journal of Spacecraft and Rockets*) will be combined and mailed separately early in 1978. In addition, papers appearing in volumes of the *Progress in Astronautics and Aeronautics* book series published in 1977 will be included. Librarians will receive one copy of the index for each subscription which they have. Any AIAA member who subscribes to one or more Journals will receive one index. Additional copies may be purchased by anyone, at $10 per copy, from the Circulation Department, AIAA, Room 730, 1290 Avenue of the Americas, New York, New York 10019. **Remittance must accompany the order.**

Ruth F. Bryans
Director, Scientific Publications